Check for updates

Synthesis of micro-mesoporous materials ZSM-5/FDU-12 and the performance of dibenzothiophene hydrodesulfurization†

Honglei Zhang,[ab] Longnian Han,‡[b] Aijun Duan, [ID] *[ac] Chunming Xu,*[a] Zhen Zhao, [ID] [a] Yuechang Wei,[a] Guiyuan Jiang,[a] Jian Liu, [ID] [a] Dong Wang[b] and Zesheng Xia[a]

The micro-mesoporous materials ZF-*x* (ZSM-5-FDU-12, *x* = SiO$_2$/Al$_2$O$_3$) with different molar ratios of SiO$_2$/Al$_2$O$_3$ were synthesized by an *in situ* nano-assembly method with the ZSM-5 precursor serving as the silica source. The physicochemical properties of the supports and the corresponding catalysts were analyzed in detail by various techniques including SEM, TEM, XRD, nitrogen physisorption, FTIR, UV-Vis, pyridine IR, Raman and XPS. The nitrogen physisorption measurement showed that the composite ZF-130 possessed excellent physical properties compared to other ZF-*x* materials. In addition, the XPS spectra displayed that catalysts NiMo/ZF-*x* showed a higher sulfurization than NiMo/FDU-12, and the NiMo/ZF-130 exhibited the highest contents of MoS$_2$ and NiMoS. In addition, DBT was employed as the probe molecule to evaluate the HDS (hydrodesulfurization) performance of the sulfide catalysts of NiMo/ZF-*x* under different weight hourly space velocities (WHSVs) 20–120 h^{-1}, while NiMo/FDU-12 was used as the reference. Furthermore, the relationship between the structure of micro-mesoporous materials and the HDS activities of catalysts was systematically evaluated. The HDS efficiencies followed the order NiMo/ZF-130 > NiMo/ZF-110 > NiMo/ZF-150 > NiMo/ZF-90 > NiMo/ZF-70 > NiMo/FDU-12 under the operation conditions of 340 °C, 4.0 MPa, and H$_2$/oil of 200 20–120 h^{-1}. Compared to other NiMo/ZF-*x* catalysts, NiMo/ZF-130 displayed the highest efficiency of DBT HDS, 96.3% at 20 h^{-1}, which could be attributed to the synergistic effects of its larger pore sizes (14.9 nm), greater specific surface area (352 m^2 g^{-1}), moderate B and L acid sites, and the highest ratios of Mo^{4+}/Mo (58%) and NiMoS/NiT (64%).

1. Introduction

Environment problems caused by vehicle emissions are serious and have attracted much worldwide attention. Sulfur-containing compounds derived from transportation fuels actually produce SO$_x$ after fuel combustion and lead to acid rain and PM2.5 particles that cause respiratory diseases. Therefore, sulfur is one of the pollutants in fuels that should be removed. Moreover, the sulfur content in diesel and gasoline needs to meet strict fuel specifications with S content lower than 10 ppm.[1] However, it is a great challenge to achieve ultra-deep desulfurization due to the increasingly heavy quality of crude oil. Fortunately, hydrodesulfurization (HDS) technology with catalysts is still one of the most effective approaches to produce

highly clean products with a low sulfur content.[2] Therefore, the preparation of a catalyst with superior performance is essential for the removal of sulfur from many materials.

Supports are one of the crucial components of catalysts that can provide a platform and accelerate the dispersion of the metal components.[3,4] The conventional Al$_2$O$_3$ carriers are widely used in the industrial hydrogenation of fuel oil and exhibits outstanding mechanical strength and hydrothermal stability. Nevertheless, its promiscuous pore structure and the lack of B acid sites are detrimental to the HDS reaction. Thus, alumino-silicate zeolites, such as ZSM-5, beta and Y, are considered as supports in the HDS process due to their high hydrothermal stability, favourable isomerization properties and particularly abundant B acid sites.[5–7]

Wu and co-workers prepared a series of metal cation-functionalized M$^+$-ZSM-5 (M$^+$ = H$^+$, Al^{3+}, Ca^{2+} and Ba^{2+}) materials and the characterization results showed that H$^+$-ZSM-5 possessed the most accessible acid sites.[6] The B acids were derived from the bridge hydroxyl groups, which connected with Al and Si atoms, and the varying ratios of B acids to L acids coincided well with the different amounts and types of metal cations.

[a] State Key Laboratory of Heavy Oil Processing, China University of Petroleum, Beijing 102249, P. R. China. E-mail: duanaijun@cup.edu.cn; xcm@cup.edu.cn

[b] CNOOC Research Institute of Oil and Petrochemicals, Beijing, 102209, China

[c] State Key Laboratory of Petrochemical Resource Processing and Process Intensification Technology, Guangxi University, Nanning, 530004, P. R. China

† Electronic supplementary information (ESI) available. See DOI: 10.1039/c7ra03679e

‡ This author has equal contribution as the first author.

Nevertheless, the low pore sizes of ZSM-5 are unfavorable for their wide application in the HDS process since a great number of larger reactant molecules is involved in the reaction systems. In order to compensate for the deficiency of microporous zeolites, mesoporous silica materials have generated much interest in the catalysis field due to their extraordinary mass transfer capabilities.[8–11]

Huirache-Acuña and Cao investigated the catalytic properties of NiMoW/Al-HMS and NiMo/TiFDU-12, and both of them displayed ideal removal efficiencies of dibenzothiophene (DBT), which were attributed to the larger pore sizes and higher specific areas of the supports, as well as the average dispersion of sulfurized metal phases.[10,11] Furthermore, NiMo/TiFDU-12 with a suitable B acid content performed better than NiMo/FDU-12 in the HDS reactivity.

Several researchers have focused on the preparation of micro-mesoporous composite materials due to the low crystallinity, inferior hydrothermal stability and poor acidity of mesoporous silica materials. Moreover, they applied these materials in various catalytic processes, and significant results were obtained under certain conditions.[12–19] Gao prepared a novel hierarchical pore material and corresponding catalyst Pt/ZSM-5-SBA-15, which possessed a porous structure and high dispersion of Pt. Thus, it showed higher hydrogenation activity than the Pt/ZSM-5 and Pt/SBA-15 separately.[13] Wu successfully synthesized a NiMo/ZSM-5-KIT-6 catalyst that revealed excellent 4,6-DMDBT HDS behavior, and the corresponding desulfurization rate is double as the conventional NiMo/Al$_2$O$_3$ catalyst. The outstanding catalytic behavior of NiMo/ZK-W was derived from the synergistic contribution of the hierarchical porous structure, which eliminated diffusion hindrances. The moderate Brönsted acid sites provided by ZSM-5 facilitated the isomerization of 4,6-DMDBT in the HYD desulfurization route and displayed an excellent hydrothermal stability, which prolonged the lifetime of the catalyst.[19]

For the HDS process, micro-mesoporous materials served as excellent supports that possessed not only good physical properties but also Lewis (L) and Brönsted (B) acid sites. The B acid sites can effectively favor the cleavages of C–S bonds, which dominate the rate of HDS. In addition, appropriate additives of Al species can prevent the active centers from agglomerating by modulating the interactions between supports and active metals, which finally facilitates the sulfurization of active components and improves the HDS efficiencies of the corresponding catalysts.[10,11,19–21]

The mesoporous silica material FDU-12, with a face-centered cubic (*Fm*3*m*) structure, has been widely used as a catalyst carrier in biotechnology, adsorption, immobilization and separation processes due to its high surface area and well-ordered pore channels with a long range.[22–25] Generally speaking, a three-dimensional interlaced channel could efficiently diminish the hindrance to diffusion in comparison with the two-dimensional straight channel with similar pore sizes. In addition, FDU-12 possesses a larger cage pore size and easily tailored pore entrance size (4–9 nm), which are significant for the mass transfer of reactants and products.

In this research, ZSM-5-FDU-12-*x* (ZF-*x*) materials combined with an MFI topological structure and an *Fm*3*m* cage-like channel structure were successfully synthesized *via* an *in situ* nano-assembling method by employing a ZSM-5 precursor as a source of silicon. The molar ratios of SiO$_2$/Al$_2$O$_3$ in ZF-*x* were controlled by adjusting the various amounts of ZSM-5 in the colloidal solution. Then, the corresponding catalysts were prepared by two-step incipient-wetness impregnation procedures and their HDS performances of DBT were evaluated under certain conditions. The properties of the materials and the sulfurized catalysts were characterized by different techniques. The results confirmed that ZF-*x* samples possessed a large pore diameter, high specific surface area and tunable acid sites. Prominent physical chemistry properties actually made it effective to disperse molybdenum species and develop MoS$_2$ and NiMoS active component phases, which were conducive to improve the HDS reactions. Moreover, the effects of SiO$_2$/Al$_2$O$_3$ ratios on the DBT HDS efficiency were explored. Then, the optimal ratio of SiO$_2$/Al$_2$O$_3$ was determined, along with the characterization of these materials to rationalize the experimental observations.

2. Experimental and characterization

2.1 Synthesis of the materials

The micro-mesoporous materials ZF-*x* (*x* = SiO$_2$/Al$_2$O$_3$) with different molar ratios of SiO$_2$/Al$_2$O$_3$ were prepared by an *in situ* nano-assembly method. First, a ZSM-5 zeolite precursor solution was synthesized with a molar ratio of 1Al$_2$O$_3$: 30SiO$_2$- : 14.7TPABr : 17NaOH : 2000H$_2$O. The specific procedure was as follows: 0.6 g of NaOH and 5.3 g TPABr were dissolved in 8 g of deionized water, and 10 g of colloidal silica was added into the previous solution with consistent stirring to obtain solution I. Solution II was derived from the mixture of 0.287 g of NaOH and 1.0 g of NaAlO$_2$ in 10 g of distilled H$_2$O. Afterwards, the homogenous gel solution was prepared by dripping solution II into solution I with persistent stirring for 4 h at ambient temperature. The aluminosilicate sol–gel solution was transferred into a polypropylene bottle and hydrothermally treated for 21 h at 443 K to obtain the ZSM-5 seed precursor. Second, ZF-*x* (*x* = 70, 90, 110, 130 and 150) was prepared by employing both a zeolite ZSM-5 seed and tetraethylorthosilicate (TEOS) as the silica source under the synergistic effect of inorganic salt additives of KCl. In the typical steps, 5 g of KCl, 2.0 g of TMB and 2.0 g of triblock copolymers EO$_{106}$PO$_{70}$EO$_{106}$ (F127, BASF), used as a textural template agent, were dissolved in 120 ml of 2 M hydrochloric acid HCl solution and stirred for 24 h. Then, 2.0 TEOS and various amounts of ZSM-5 seed were added into the mixture and stirred for another 24 h at a constant temperature of 293 K, and the solution was transferred into a Teflon bottle and heated for 24 h at 373 K. The resultant mixture was filtered, washed and dried at 253 K to obtain the as-synthesized samples, which needed to be calcined for 6 h at 823 K to obtain micro-mesoporous materials, ZF-*x*, after the removal of the F127 template.

Zeolite ZSM-5 with high crystallinity was prepared by the same method mentioned above by extending the crystallization time to 48 h and was taken as a reference.

The pure mesoporous material FDU-12 was obtained under a bath temperature of 293 K, as described in the literature.[22]

2.2 Preparation of the catalysts

H-ZSM-5 and H-ZF-x were pretreated twice by ammonium exchange with the mass ratio of 1 support : 3NH$_4$Cl : 30H$_2$O, and the catalysts NiMo/ZSM-5 and NiMo/ZF-x were prepared stepwise *via* a two-step incipient wetness method with aqueous solutions of ((NH$_4$)$_6$Mo$_7$O$_{24}$·4H$_2$O) and (Ni(NO$_3$)$_2$·6H$_2$O). The samples were filtrated, washed, dried and calcined at 823 K for 6 h after each ammonium exchange and impregnation. NiMo/FDU-12 was prepared in the same manner with the previously mentioned steps without ammonia exchange, and all catalysts contained 10 wt% MoO$_3$ and 3.5 wt% NiO.

2.3 Characterization

Wide angle (2θ = 5–50°) and low angle (2θ = 0.4–5°) X-ray diffraction (XRD) data were measured on the Bruker D8 advance system with Cu Kα radiation at 40 kV and 50 mA, and scan speeds of 1° min^{-1} and 2.4° min^{-1}.

The physicochemical properties of materials and catalysts were acquired with the Micromeritics TriStar II 3020 porosimetry analyzer at 77 K. The samples were outgassed at 350 °C for 4 h in a vacuum environment before being adsorbed by N$_2$. The specific surface areas and pore size distributions were calculated using the Brunauer–Emmett–Teller (BET) method and Barrett–Joyner–Halenda (BJH) method with an adsorption branch.

Transmission electron microscopy (TEM) images were taken on a JEOL JEM 2100 instrument with an accelerating voltage of 200 kV to obtain the channel structure of supports.

The morphologies of samples were obtained by emission scanning electron microscopy (SEM) on a Quanta 200F instrument under an acceleration voltage of 20 kV.

UV-Vis diffuse reflectance spectroscopy (UV-Vis DRS) results were collected using a Hitachi U-4100 device at the wavelength range from 200 nm to 800 nm with the integration sphere diffuse reflectance attachment.

Raman spectra with wavenumbers of 1200–200 cm^{-1} were collected on a Renishaw Raman InVia Microscope (Spectra-Physics model 163) with a spectral resolution of 2 cm^{-1}. A He/Cd laser line of 325 nm was employed as the excitation source with an output of 20 mW, and the laser spot size was approximately 1–2 µm with a power of 3.6 mW.

Fourier transform infrared (FTIR) absorbance spectra were recorded using a FTS-3000 spectrophotometer to obtain information on the acid strength and content of the catalysts. The catalysts were dehydrated at 500 °C for 5 h under vacuum before being adsorbed by purified pyridine vapor. B and L acid sites could be distinguished according to different outgassing temperatures, and the total acid content was calculated by IMEC(B) = 1.67 cm µmol^{-1} and IMEC(L) = 2.22 cm µmol^{-1}.[26]

X-ray photoelectron spectroscopy (XPS) examination of the sulfurized catalysts was performed on a Perkin Elmer PHI-1600 ESCA spectrometer using Al Kα radiation (40 eV, <10–9 mbar). The sulfurized catalysts were left in a cyclohexane solution to prevent oxidation and pressed into a flake shape.

2.4 Catalytic activity

A 0.5 g amount of catalyst was loaded in the continuous flowing tubular fixed-bed inconel reactor (D = 9 mm, L = 50 mm) and presulfurized with a cyclohexane solution of 2.5 wt% CS$_2$ at 340 °C, 4 MPa of H$_2$ pressure and volume ratio of 200 for H$_2$/oil for 4 h after being shaped into solid particles of 40–60 mesh. Then, the HDS performance of DBT of all catalysts was estimated employing DBT dissolved in cyclohexane as reaction raw feed (500 ppm S) under the same reaction conditions as that of presulfurization except for modulation of the various WHSV values of 20–150 h^{-1}. The S content of the products was detected by a sulfur and nitrogen analyzer (RPP-2000SN, Taizhou Central Analytical Instruments Company, China), and the desulfurization rate was calculated by the following equation:

$$\text{HDS efficiency} = (S_\text{f} - S_\text{p})/S_\text{f} \times 100\%.$$

where S_f and S_p are defined as the sulfur contents of the feed and products, respectively.

3. Results and discussion

3.1 Characterization of materials and catalysts

3.1.1 XRD characterization of the materials. The wide angle and low angle XRD patterns of ZF-x with different SiO$_2$/Al$_2$O$_3$ molar ratios are shown in Fig. 1(A) and (B), respectively. All hierarchically porous materials exhibited the characteristic diffraction peaks at a 2θ of 8–10° and 20–25° (Fig. 1(A)), which were attributed to the MFI topological structure in the ZSM-5 zeolite. However, the intervallic intensity contrast of peaks between ZF-x materials and ZSM-5 zeolite was derived from the incorporated ZSM-5 seeds, which consisted of only primary and secondary structural units instead of the finished ZSM-5 zeolite.[13,27] It was found that the intensities of the characteristic peaks at 8–10° and 20–25° gradually decreased with the diminution of the ZSM-5 precursor. Fortunately, the discernible peaks indexed as (111), (220), (311), (331) and (442) reflections of the *Fm3m* structure could be clearly distinguished as the
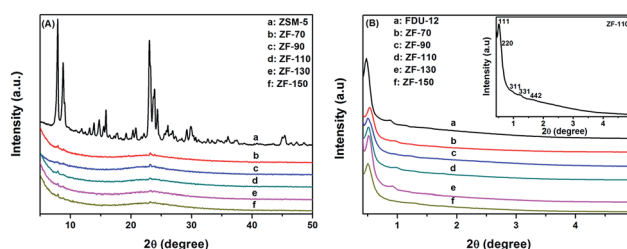

Fig. 1 XRD patterns of the series of materials at wide angle (A) and low angle (B) regions.

response of the ZF-130 sample (Fig. 1(B) inset).[22] Moreover, all ZF-x composites showed clear and typical signals as the pure mesoporous silica sample FDU-12 at 0.4–2° in Fig. 1(B), indicating that the ZF-x samples had the same face-centered cubic texture (*Fm3m*), highly ordered symmetry and regular mesoporous structure after the incorporation of the ZSM-5 seed into the framework of FDU-12.

3.1.2 FTIR of the materials. FTIR is a reliable method to measure the configuration and conformation of target atoms in materials (Fig. 2). The band near 801 cm^{-1} was present in all samples and was assigned to the symmetric Si–O–Si stretching vibration.[28] Pure silica FDU-12 also showed bands at 460 cm^{-1} and 1082 cm^{-1}, which belonged to the bending and antisymmetric stretching modes of Si–O–Si, respectively. Moreover, the corresponding characteristic bands at 454 cm^{-1} and 1097 cm^{-1} were observed in the composite material ZF-130, which were consistent with those in the ZSM-5 zeolite.[29] The above-mentioned peak-shifts occurring in ZF-130 compared to FDU-12 were caused by the incorporation of ZSM-5 seeds into the wall of the composite material and consequently changed the skeleton phases. The coordination states of Si–O–Si over the composite ZF-130 were the same as the ZSM-5 rather than the FDU-12, which confirmed that the frameworks of the composite material ZF-130 were formed by the ZSM-5 precursors. Similar to the ZSM-5 zeolite, the sample ZF-130 gave rise to the representative signal but with a lower intensity at 547 cm^{-1}, which was attributed to the bending vibration of five-membered rings of T–O–T (T = Si or Al) in the MFI topological structure.[28] Apparently, the peak at 547 cm^{-1} did not exist in the pure mesoporous material FDU-12, which further illustrates the structural modification of the framework in the composite ZF-130 relative to the FDU-12 sample. In particular, the band observed at 958 cm^{-1} could be ascribed to the asymmetric stretching mode of silicon hydroxyl groups on the surfaces of the support.

3.1.3 SEM of the materials. The morphologies of pure silica FDU-12 and the composite material ZF-130 with a certain content of ZSM-5 seeds were examined using field emission scanning electron microscopy (SEM). As shown in Fig. 3, the calcined sample ZF-130 revealed amorphous polyhedral shapes instead of regular discrete hexagonal prisms presented in FDU-12, and the scattered particles with an ellipsoid appearance also were observed for the ZSM-5 zeolite. In general, the Na$^+$ cation
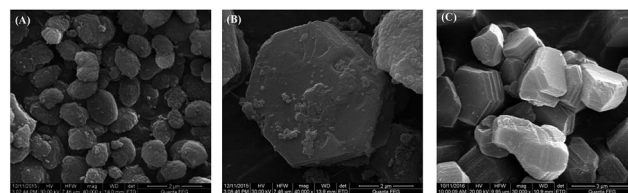

Fig. 3 SEM images of the calcined samples (A) ZSM-5, (B) FDU-12 and (C) ZF-130.

has a more remarkable ability to dehydrate the methyl group on PEO and particularly the PPO segments of amphipathic polymer F127 than K$^+$ due to their different ionic radius and polarization capabilities under their equal charges, which induces a stronger hydrophobic ability of F127, following easier assembly of micelles.[30,31] Clearly, the critical micelle temperature (CMT) and critical micelle temperature concentration (CMC) of segmented copolymer F127 becomes lower. Then, the micelles tend to transform into other shapes due to both hydration and salting-out effects of Na$^+$.[32] As a result, irregular morphologies of ZF-130 are observed (Fig. 3(C)). Furthermore, the micro-mesoporous material of ZF-130 shows a rougher solid surface than the pure FDU-12 after the incorporation of ZSM-5 precursors. Fortunately, there are no isolated ZSM-5 crystals in the SEM images. Therefore, it can be concluded that the frameworks of ZF-x micro-mesoporous materials were constructed by the primary and second units of ZSM-5, rather than by mechanical mixing of the silica-based mesoporous materials and ZSM-5 crystals.

3.1.4 Nitrogen physisorption of the materials and catalysts. Fig. 4(A) shows the N$_2$ adsorption–desorption isotherm patterns of zeolite ZSM-5, mesoporous silica FDU-12 and micro-mesoporous materials of ZF-x with various ratios of SiO$_2$/Al$_2$O$_3$, and the corresponding pore diameter distribution curves are shown in Fig. 4(B). All ZF-x samples exhibit the same classic H2, type-IV hysteresis loop like the mesoporous material FDU-12, which possesses a cage-like mesoporous texture with multiple necks.[33] Moreover, the sharp changes in the N$_2$ adsorption observed for all materials at the relative P/P_o ranges from 0.8 to 0.85 and from 0.45 to 0.5 signify the existence of unified cavities and necks. Moreover, the corresponding steep positions are actually determined by the diameters of the cavities and windows according to capillary condensation theory.[34] Therefore, the various jump positions located in the adsorption
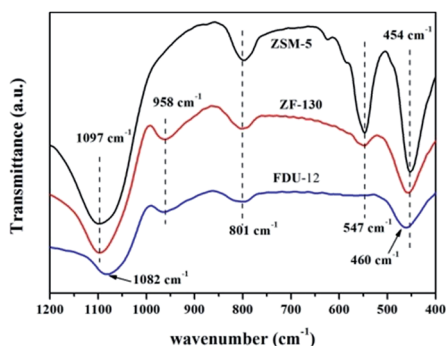

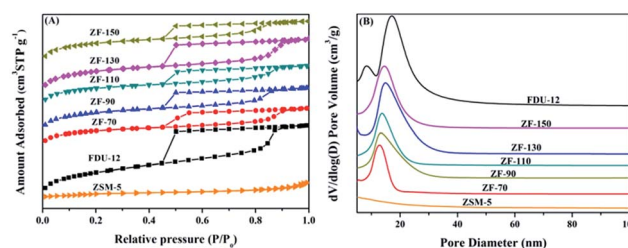**Fig. 2** FT-IR spectra of ZSM-5, FDU-12 and ZF-130.

Fig. 4 N$_2$ adsorption–desorption curves (A) and pore size distributions (B) of various materials.

and desorption branches, mean their different pore sizes of cage and entrance. Moreover, all pore size distribution curves that originate from the adsorption branches are shown in Fig. 4(B). The concentrated pore distributions also demonstrate that ZF-x materials possess a regular and long-range, well-ordered pore structure, which agree with XRD and TEM results. Moreover, the particular structural parameters of the supports and catalysts are displayed in Table 1. All composite materials of ZF-x have relatively few smaller pore sizes than the pure silica sample of FDU-12 (17.3 nm). It is noteworthy that the pore sizes of ZF-x spontaneously decrease along with increasing amounts of the ZSM-5 nanocrystal, indicating that the wall of the hole was thicker due to the incorporation of ZSM-5 textural units into the framework.[12,13] The catalyst NiMo/ZSM-5 had the lowest specific surface area (207 m^2 g^{-1}) due to the microporous zeolite carrier, while the relatively lower mesoporous volume (0.17 cm^3 g^{-1}) should be contributed by the inter-particle pores. Compared to other ZF-x samples, the aluminosilicate material ZF-130 shows the largest specific surface area (760 m^2 g^{-1}) and mesoporous volume (0.58 cm^3 g^{-1}), which facilitate the dispersion of active metal components on the support. Generally, the pore size, cumulative pore volume and specific surface area of the catalysts decrease to different extents after the loading of Ni and Mo species, which are ascribed to the blockage of the pore caused by the metallic oxides during the impregnation process. However, the catalysts NiMo/ZF-x still had lager pores to facilitate mass transfer of the heterocyclic sulfide DBT.

3.1.5   TEM of the materials. Fig. 5 shows the TEM images of pure silica FDU-12 recorded at the (111) direction and the composite ZF-130 taken along with (111), (110), (100) and (211) directions, which clearly demonstrate that ZF-130 has the characteristic *Fm3m* structure and long range, well-ordered mesochannels.[22,35,36] Fig. 5(B) clearly shows a similar view of the (111) crystal face in ZF-130 as FDU-12 (Fig. 5(A)), which is correlated to their typical peaks of low angle XRD spectra with the same peak position but different intensities. Regular crystal
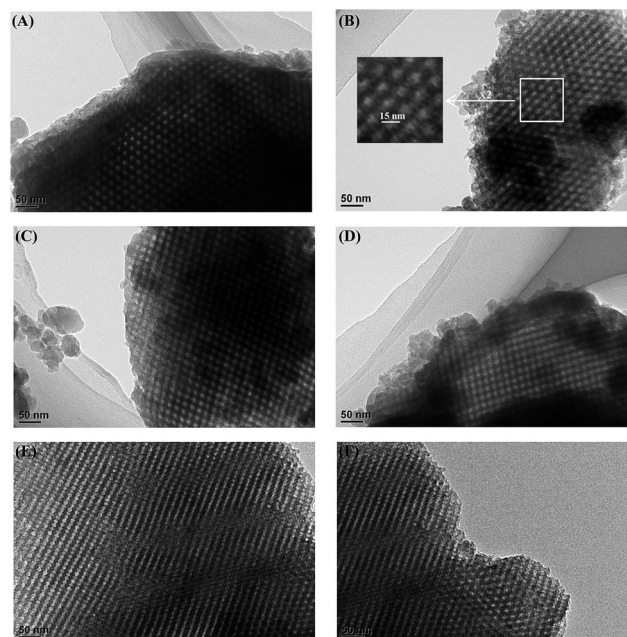

Fig. 5   TEM images of calcined materials (A) FDU-12 viewed from the (111) direction, and ZF-130 viewed from (B) (111), (C) (110), (D) (100), (E) and (F) (211) directions.

lattices over a large area derived from the (110), (100) and (211) directions are also visible in Fig. 5. However, to some extent, the slightly impaired mesoporous structure over narrow regions was inevitable as observed in the white rectangle of Fig. 5(E) and (F). It can essentially be interpreted as the incorporation of excessive ZSM-5 precursors into the framework of mesoporous silica, although it was difficult to distinguish the MFI topology phase by TEM technique. In addition, the ink bottle-type pore structure in the ZF-130 was coincident with the results from the N$_2$ adsorption–desorption isotherm patterns. Nevertheless, the negligible deviation of the pore sizes evaluated by the TEM (estimated about 15 nm as Fig. 5(B) inset) and BJH method (15.3

Table 1   The structural parameters of the synthesized materials and the corresponding catalysts

Samples	S_{BET}[a] (m^2 g^{-1})	V_t[b] (cm^3 g^{-1})	V_{mes}[c] (cm^3 g^{-1})	V_{mic}[d] (cm^3 g^{-1})	d_{BJH}[e] (nm)
ZSM-5	304	0.21	0.18	0.09	
FDU-12	789	0.79	0.76	0.02	17.3
ZF-70	564	0.47	0.40	0.04	12.4
ZF-90	697	0.55	0.44	0.05	13.4
ZF-110	648	0.51	0.39	0.05	14.0
ZF-130	760	0.63	0.58	0.04	15.3
ZF-150	733	0.54	0.39	0.06	15.4
NiMo/ZSM-5	169	0.12	0.11	0.04	—
NiMo/FDU-12	391	0.59	0.57	0.01	17.0
NiMo/ZF-70	259	0.31	0.28	0.04	11.0
NiMo/ZF-90	283	0.35	0.29	0.02	11.7
NiMo/ZF-110	317	0.35	0.34	0.03	12.5
NiMo/ZF-130	352	0.46	0.45	0.02	14.9
NiMo/ZF-150	298	0.37	0.36	0.03	13.8

[a] Calculated by BET method. [b] The total pore volume was obtained at a relative pressure of 0.99. [c] Calculated using BJH method. [d] Calculated using the *t*-plot method. [e] Mesopore diameter was calculated using BJH method.

nm) derived from the image contrast showed that there was no exact agreement between the white disk and pore diameter because of the thick stack of the samples.[22]

3.1.6 Py-IR of the materials. Pyridine is usually adopted as the probe molecule to investigate the amount of acidic sites because of its characteristic interaction with different types of acid sites.[37]

Fig. 6 displays the pyridine IR spectra of catalysts on absorbing pyridine after desorbing at 200 °C and 300 °C. As shown in Fig. 6(A), all NiMo/ZF-x catalysts showed a similar band at 1545 cm^{-1} as NiMo/ZSM-5, which was attributed to the B acid sites. However, there was no B acid located in NiMo/FDU-12 according to the absence of a characteristic signal at 1545 cm^{-1}.[38] The bands appearing at 1449 cm^{-1} and 1608 cm^{-1} were ascribed to the interactions of pyridine with L acid sites, while slight shifts were observed in NiMo/ZSM-5.[39] Moreover, NiMo/ZSM-5 exhibited partially overlapped bands (at about 1630 cm^{-1}) of B and L acid sites. In addition, the typical band present at 1489 cm^{-1} was also due to the combination of B and L acid sites.[38,39]

Table 2 lists the distribution data of acid sites in the various catalysts. After desorbing pyridine at 200 °C, NiMo/ZSM-5 had the highest B acid content, while a few of the B acid sites were attached on the composite catalysts of NiMo/ZF-x due to the introduction of Al species. Furthermore, not only the total amount of acids, but also more L acids were generated in NiMo/ZF-x rather than in NiMo/FDU-12 at 200 °C and 300 °C. The total amount of B acid sites followed the order NiMo/ZSM-5 > NiMo/ZF-70 > NiMo/ZF-90 > NiMo/ZF-110 > NiMo/ZF-130 > NiMo/ZF-150. Wu[19] demonstrated that moderate B acid sites facilitated the breakage of the C–S bond and finally accelerated the HDS reaction. Nevertheless, the medium and strong B acid sites did not exist in the series of NiMo/ZF-x catalysts as those obtained at 350 °C.

3.1.7 UV-Vis DRS of the catalysts. Fig. 7 shows the UV-Vis DRS results of porous catalysts with different amounts of crystalline ZSM-5. UV-vis spectra in the region of 200–800 nm reflect the nature of the chemical forms and polymerization states of Mo oxide species on the surface of the supports. The apparent absorption signals in the 200–390 nm region were present in all NiMo catalysts, which confirmed the presence of a ligand-to-metal change transfer band (LMCT) $O^{2-} \rightarrow Mo^{6+}$.[40] Moreover, the characteristic band positions primarily depended on the coordination environments of Mo components. Specifically, the

Table 2 Amounts of B and L acid sites determined by pyridine-FTIR of different catalysts

| Catalysts | Amount of acid sites (µmol g^{-1}) | | | | | |
| | 200 °C | | | 350 °C | | |
	B	L	L + B	B	L	L + B
NiMo/ZSM-5	53.4	61.0	114.4	26.4	29.8	56.2
NiMo/FDU-12	—	60.5	60.5	—	25.2	25.2
NiMo/ZF-70	11.7	96.1	107.8	—	42.6	42.6
NiMo/ZF-90	9.0	82.2	91.2	—	35.7	35.7
NiMo/ZF-110	8.8	75.6	84.4	—	31.3	31.3
NiMo/ZF-130	7.5	78.4	85.9	—	33.8	33.8
NiMo/ZF-150	6.4	65.8	72.2	—	30.4	30.4

bands recorded at about 260–285 nm were ascribed to the isolated tetrahedral molybdate, while the higher wavelength bands (290–335 nm) coincided with the octahedrally-coordinated Mo oxide species.[41] All catalysts displayed characteristic peaks of two types of coordinated Mo species in the wavelength range of 260–335 nm and the secondary peak centered on 225 nm, which was the integrated result of both tetrahedral and octahedral molybdate species. The strength and width of the typical peaks observed in various samples slightly changed with different amounts of Al additives, whereas the relatively higher ratio of Mo (Oh) species still remained over the detected catalysts, which facilitated the formation of easily reduced sulfur vacancies and consequently resulted in excellent hydrodesulfurization efficiencies.

3.1.8 Raman spectra of the catalysts. UV Raman technique, because of its high detection sensitivity, is often applied in investigating the coordination symmetry of frameworks in materials and the phase state of active metal oxides. Fig. 8 shows the Raman spectra (325 nm) of the series of oxidized NiMo/ZF-x catalysts. The catalyst NiMo/FDU-12 exhibited the typical vibrations of chemical bonds at 494 cm^{-1}, 837 cm^{-1}, 947 cm^{-1} and 951 cm^{-1} (Fig. 8 inset). Accordingly, the signals detected at 494 cm^{-1} and 837 cm^{-1} were assigned to the tetrahedral structure vibration of O_3SiOH and the symmetric stretch
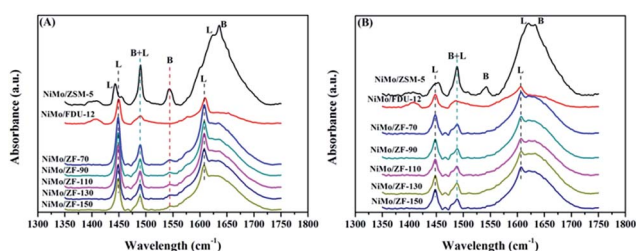

Fig. 6 FTIR spectra of various catalysts on absorbing pyridine after degassing at (A) 200 °C and (B) 350 °C.
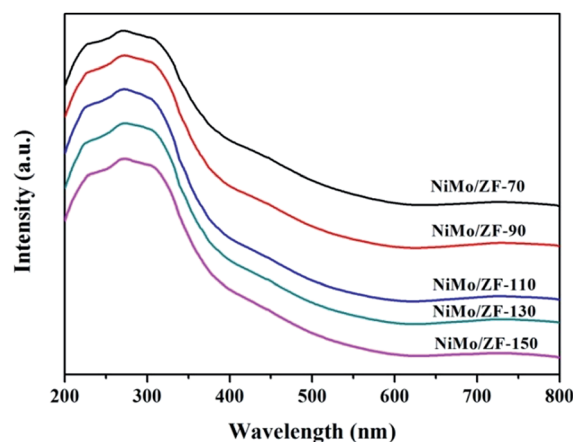
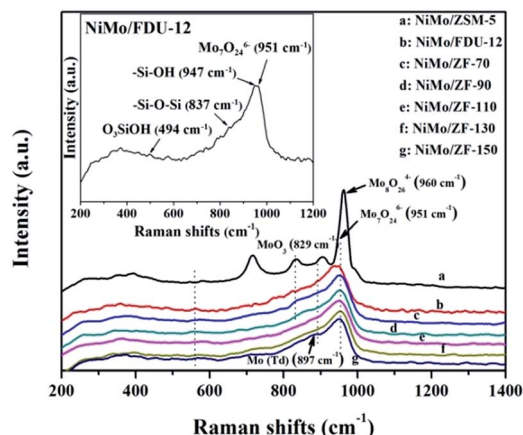

Fig. 7 UV-Vis DRS spectra of the oxidized catalysts.

Fig. 8 Raman spectra of different oxidized catalysts.

movement of Si–O–Si separately.[42,43] It was noticeable that the stronger peak located around 950 cm^{-1} was divided into two parallel and distinguished peaks. The peak at 947 cm^{-1} was attributed to the stretching vibration of the hydroxyl group (Si–OH) along the length of the surface of the materials and another one emerged at 951 cm^{-1} that was derived from the stretching vibration of Mo=O located in the extreme of $Mo_7O_{24}^{6-}$.[44–46] However, the single typical peak at 951 cm^{-1} could be distinctly observed in all NiMo supported aluminosilicate catalysts in Fig. 8, indicating that the hydroxyl groups of composite materials might be decorated to be Si–O–Al linked phases due to the incorporation of Al into the framework (FT-IR results in Fig. 2). Simultaneously, the wide characteristic peaks at 951 cm^{-1} confirmed the presence of a favorable dispersion of $Mo_7O_{24}^{6-}$ on the NiMo/FDU-12 and NiMo/ZF-x catalysts. In general, it was easier to sulfurize $Mo_7O_{24}^{6-}$ species due to their relatively weak interactions with supports, which appreciably favored the improvement of the degree of sulfurization of Mo species.[47,48] The peak at 829 cm^{-1} was attributed to Mo–O–Mo in the orthorhombic MoO_3. The slightly aggregated MoO_3 on the surface of NiMo/ZF-x (x = 70, 90) should be caused by the introduction of redundant Al species. And NiMo/ZSM-5 has higher content of Al species, so it shows a relatively stronger characteristic peak of aggregated MoO_3.[49] Moreover, only NiMo/ZSM-5 displayed a Raman signal at 960 cm^{-1}, which was associated with the vibrational mode of $Mo_8O_{26}^{4-}$, supporting the intensive chemical effects between Mo species and microporous ZSM-5 zeolite.[50] The typical peak situated at 897 cm^{-1} was clearly observed in NiMo/ZF-150, but absent in NiMo/ZF-130, was ascribed to the interaction of tetrahedral Mo species, which was inactive for HDS.[47,51] Overall, the characteristic Raman spectra of NiMo/ZF-130 were distinct from those of NiMo/ZSM-5 and NiMo/FDU-12. Moreover, it can be deduced that NiMo/ZF-130, with the higher ratio of $Mo_7O_{24}^{6-}$ species, might possess extraordinary HDS efficiency.

3.1.9 XPS of the catalysts. The XPS technique was used to analyze the Mo species (Mo^{4+}, Mo^{5+}, and Mo^{6+}) dispersions on the surface of the sulfurized catalysts NiMo/FDU-12 and NiMo/ZF-x with different amounts of Al. The Mo XPS spectral peaks

and the calculated data are shown in Fig. 9 and Table 3, respectively. The characteristic peaks of Mo^{4+} (MoS_2) were divided into two signals fit at 228.6 ± 0.1 eV and 231.7 ± 0.1 eV, which belonged to Mo^{4+} ($3d_{3/2}$) and Mo^{4+} ($3d_{5/2}$), respectively, whereas Mo^{5+} ($3d_{3/2}$, $3d_{5/2}$) appeared at 229.9 ± 0.1 eV and 233.1 ± 0.1 eV, and Mo^{6+} ($3d_{3/2}$, $3d_{5/2}$) appeared at 232.3 ± 0.1 eV and 235.5 ± 0.1 eV.[52] Simultaneously, the BE (binding energy) of 225.8 eV corresponded to S 2s.[52] From Table 3, the contents of various Mo species were calculated from their relative area percentages from XPS peaks, and the order of Mo^{4+} in the catalysts was NiMo/ZF-130 > NiMo/ZF-110 > NiMo/ZF-150 > NiMo/FDU-12. All Mo oxide species in the supported composite materials were more prone to be sulfurized and exhibited higher sulfurization than the pure silica NiMo/FDU-12. These observations could be because the interactions between Mo species and the supports changed in a favorable direction due to the introduction of Al atoms and the accompanied electric effects. However, it is noteworthy that NiMo/ZF-130 displayed the highest ratio not only in the total content of Mo^{4+} (58%), but also in Mo^{4+} ($3d_{3/2}$) (55%) and Mo^{4+} ($3d_{5/2}$) (23%), which could be attributed to its moderate acidity and larger specific surface area, pore size and pore volume. This phenomenon also demonstrated that the facile sulfurization was derived from $Mo_7O_{24}^{6-}$ instead of MoO_3 according to the Raman data. In the HDS reaction, taking the significant role of Mo^{4+} (MoS_2) into consideration, the composite catalyst NiMo/ZF-130, with the largest S_M^b value, might exhibit an excellent efficiency for the removal of DBT.

For the sulfurized catalysts, the Ni 2p XPS spectral curves were caused by the NiS, NiO and NiMoS species.[53] Moreover, the Ni 2p XPS spectra of the catalysts NiMo/FDU-12 and NiMo/ZF-x are shown in Fig. 10. All Ni 2p envelopes disintegrated into three fitted curves located at BE 873.6 ± 0.1 eV, 862.2 ± 0.1 eV and 855.8 ± 0.1 eV, which could be ascribed to NiS ($2p_{1/2}$), NiO and NiMoS phases, respectively.[54,55] In addition, the detailed information of various Ni species is summarized in Table 4. The ratio of NiMoS/Ni$_{total}$ followed the order NiMo/ZF-130 > NiMo/ZF-150 > NiMo/ZF-110 > NiMo/FDU-12. Compared to NiO and NiS, NiMoS phases were preferable and more capable of driving the
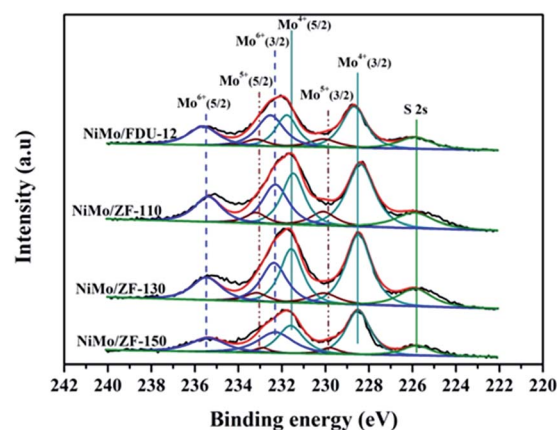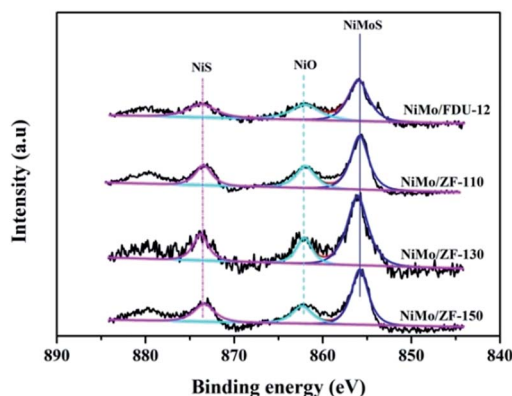

Fig. 9 Mo 3d XPS spectra of the sulfurized catalysts NiMo/FDU-12 and NiMo/ZF-x with different SiO_2/Al_2O_3 ratios.

Table 3 Mo 3d XPS analysis results of the sulfurized NiMo supported catalysts

Catalysts	Mo^{4+}		Mo^{5+}		Mo^{6+}		S_M^{b}
	ar^a% (228.6 eV)	ar% (231.6 eV)	ar% (229.9 eV)	ar% (233.1 eV)	ar% (232.3 eV)	ar% (235.5 eV)	
NiMo/FDU-12	29	19	9	4	24	15	48
NiMo/ZF-110	33	22	6	5	20	14	55
NiMo/ZF-130	35	23	6	4	20	12	58
NiMo/ZF-150	33	21	5	3	23	15	54

^{a} ar% means the area percent of the XPS peak. ^{b} S_M = Mo$_{sulfurization}$ = Mo^{4+}/(Mo^{4+} + Mo^{5+} + Mo^{6+}).

Fig. 10 Ni 2p XPS spectra of various sulfurized catalysts.

HDS reaction. The lowest ratio of NiMoS/Ni$_{total}$, but the largest value of NiO and NiS, could be obtained in the NiMo/FDU-12 catalyst due to the lack of ZSM-5 structural units according to the FT-IR analysis. And the highest ratio of NiMoS/Ni$_{total}$ observed in the NiMo/ZF-130, which corresponds well to its excellent physicochemical properties, can achieve to 64%.

3.2 Catalytic performance of the catalysts

It is extremely important to remove the heterocyclic sulfur compound DBT contained in diesel in order to produce ultra clean fuel. Hence, DBT served as the probe molecule and was used in evaluating the HDS efficiencies of catalysts over different carriers of FDU-12 and ZF-x. All catalysts exhibited higher HDS efficiencies than the pure mesoporous catalyst NiMo/FDU-12 as shown in Fig. 11. The approximate trend was NiMo/ZF-130 > NiMo/ZF-110 > NiMo/ZF-150 > NiMo/ZF-90 > NiMo/ZF-70 > NiMo/FDU-12, and the HDS efficiencies of all

catalysts gradually decreased with an increase in WHSV, which was detrimental to the reaction time. The catalyst NiMo/ZF-130 displayed a higher specific surface area and lager pore sizes. The former high specific surface area was achieved by a suitable dispersion of Mo species. The larger pore sizes decreased the diffusion resistance of DBT. Moreover, the highest HDS ratio was observed in the NiMo/ZF-130 with a WHSV range from 20 h^{-1} to 120 h^{-1} rather than in the other composite catalysts of NiMo/ZF-x. The catalyst NiMo/ZF-130 showed higher HDS efficiencies than NiMo/C-MA in the range of 20 h^{-1} to 100 h^{-1} due to their differences in physical and chemical properties. The absence of B acid sites in the catalyst NiMo/C-MA made it difficult to break the C–S bond in the heterocyclic sulphides, and the narrower pore channels increased the diffusion resistance of the larger-sized reactants; hence, NiMo/C-MA could not achieve the desired HDS performance.[56] The catalyst NiMo/FDU-12 possessed the largest superficial area and pore volume, which could afford an excellent platform for the dispersion of active metal species and eliminate the mass transfer resistance of DBT, respectively. However, the catalyst NiMo/FDU-12 displayed the lowest performance for the HDS reaction.

Actually, not only physical properties, but also the acidity (B + L) and the Al species in the catalysts had synergetic effects on the HDS reaction. The L acid sites favored the hydrogenation of DBT on the surface of the catalysts. Moreover, the B acid sites accelerated the breakage of the C–S bond in the DBT, which determined the rates of HDS in both DDS (direct desulphurization) and HYD (hydrogenation) reaction processes. As for the absence of B acid sites, it is resonable that catalyst NiMo/FDU-12 has the lowest removal rate of DBT under the uniform reaction conditions. However, the excessive B acid sites were inclined to induce carbon depositions in the catalysts, which covered the active metal sites and prevented them from making

Table 4 Ni 2p XPS analysis results of different sulfurized catalysts

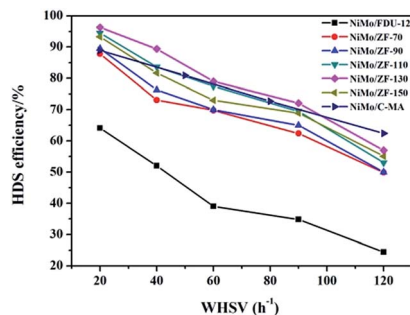| Catalysts	NiS/ar^a% (873.6 eV)	NiO/ar^a% (862.2 eV)	NiMoS/ar^a% (855.8 eV)
NiMo/FDU-12	22	27	49
NiMo/ZF-110	22	26	52
NiMo/ZF-130	18	18	64
NiMo/ZF-150	19	25	56

^{a} ar% means the area percent of the XPS peak.

Fig. 11 DBT HDS efficiency over the catalysts NiMo/FDU-12, NiMo/ZF-*x* and NiMo/C-MA (commercial mesoporous γ-Al₂O₃) at various WHSV values.

contact with DBT. As a result, the catalyst NiMo/ZF-70 showed a lower HDS efficiency of DBT at 20 h⁻¹, ~87.8%. The catalyst NiMo/ZF-130 exhibited the appropriate content of B and L acid sites. The Al species were incorporated into the frameworks and fixed on the surface of the composite catalysts NiMo/ZF-*x*. As an electronic accelerator, the Al species could adjust the interactions between the active metal components and the supports, and facilitate the dispersion of metal species over the catalysts. Nevertheless, the excessive Al species led to the shrinkage of the pores, which was unfavorable for the metal dispersion and the utilization of Mo species to a certain extent. The NiMo supported catalyst with a SiO_2/Al_2O_3 of 130 possessed a suitable Al content, which optimized the interactions between the NiMo species and the supports. Therefore, the catalyst NiMo/ZF-130 exhibited the lager content of $Mo_7O_{24}^{6-}$ which was easier to sulfurize. Also, NiMo/ZF-130 had the highest ratios of Mo^{4+}/Mo_{total} and $NiMoS/Ni_{total}$, which was in agreement with the results of the XPS spectra. Sufficient active sites in MoS_2 could effectively accomplish the thorough removal of sulfides.

In summary, NiMo/ZF-130 was more capable of eliminating DBT than other catalysts under the same reaction conditions, and the HDS efficiency approached 96.3% at 20 h⁻¹.

4. Conclusions

The hierarchical, porous composites of ZF-*x* with various ratios of SiO_2/Al_2O_3 were successfully synthesized according to an *in situ*, nano-assembly method using ZSM-5 microporous crystals as the source of silica. Wide-angle XRD spectra confirmed that a MFI topological structure was present in the ZF-*x* samples. Especially, the analysis of FTIR showed the typical vibration of five-membered rings of T–O–T (T = Al or Si), and the pyridine IR results supported the existence of certain B acid sites. Moreover, solid particles of ZSM-5 crystallographic seeds were not observed in the SEM images, illustrating that ZSM-5 structural units were chemically incorporated into the framework of carriers of ZF-*x* rather than in the mechanical mixing. Moreover, nitrogen physisorption analysis showed that micro-mesoporous materials of ZF-*x* not only had a *Fm3m* structure similar to that of the pure mesoporous silica FDU-12, but the corresponding catalysts and symmetrical crystal lattices with a long-range still

remained in the ZF-130 composite, as shown in the TEM images. The Raman spectral peaks showed that there was no agglomerated MoO_3 clusters on the surface of NiMo/FDU-12 and NiMo/ZF-130. It was noted that the sulfurized, composite catalysts NiMo/ZF-*x* exhibited higher sulfurization than NiMo/FDU-12, and the catalyst NiMo/ZF-130 had the highest ratio of Mo^{4+}/Mo_{total} and $NiMoS/Ni_{total}$ as shown in the XPS spectra. The specific HDS efficiency followed the order NiMo/ZF-130 > NiMo/ZF-110 > NiMo/ZF-150 > NiMo/ZF-90 > NiMo/ZF-70 > NiMo/FDU-12. Apparently, the catalyst NiMo/ZF-130 exhibited the highest efficiency (96.3%) of DBT HDS at 20 h⁻¹ due to its superior physicochemical properties. The larger specific surface area and pore sizes of the catalyst NiMo/ZF-130 could promote the good dispersion of Mo species on the surface of supports and decrease the diffusion resistance of DBT reactants inside the channels, respectively. In addition, the moderate B acid sites, the largest MoS_2 and NiMoS active phases could accelerate the HDS reaction. Most importantly, the composites of ZF-*x* actually combined the advantages of microporous zeolites and mesoporous materials, and the corresponding catalysts played a significant role in the desulfurization of fuel oil.

Acknowledgements

Notes and references

1 S. Velu, S. Watanabe, X. Ma and C. S. Song, *Appl. Catal., B*, 2003, **41**, 207–238.
2 F. Trejo, M. S. Rana and J. Ancheyta, *Catal. Today*, 2008, **2**, 327–336.
3 Y. Shen, T. Sun and J. Jia, *RSC Adv.*, 2012, **2**, 3123–3132.
4 J. Hu, Z. Zhang and F. Wang, *RSC Adv.*, 2016, **6**, 101544–101551.
5 S. Saravanamurugan, M. Paniagua, J. A. Melero and A. Riisager, *J. Am. Chem. Soc.*, 2013, **135**, 5246–5249.
6 W. Wu and E. Weitz, *Appl. Surf. Sci.*, 2014, **1**, 405–415.
7 H. P. Winoto, B. S. Ahn and J. Jae, *J. Ind. Eng. Chem.*, 2016, **40**, 62–71.
8 L. Y. Han, Y. Luo, J. Liu and Z. Zhao, *Ind. Catal.*, 2011, **11**, 46–50.
9 J. Liu, L. H. Yu, Z. Zhao, Y. S. Chen, P. Y. Zhu, C. Yan and Y. Luo, *J. Catal.*, 2012, **1**, 134–144.
10 R. Huirache-Acuña, B. Pawelec, C. V. Loricera, E. M. Rivera-Muñoz, R. Nava, B. Torres and J. L. G. Fierro, *Appl. Catal., B*, 2012, **125**, 473–485.
11 Z. K. Cao, A. J. Duan, Z. Zhao, J. M. Li, Y. C. Wei, G. Y. Jiang and J. Liu, *J. Mater. Chem. A*, 2014, **46**, 19738–19749.
12 D. W. Gao, A. J. Duan, X. Zhang, K. B. Chi and Z. Zhao, *J. Mater. Chem. A*, 2015, **32**, 16501–16512.

13 D. W. Gao, A. M. Zheng, X. Zhang, H. Sun, X. P. Dai and A. J. Duan, *Nanoscale*, 2015, **25**, 10918–10924.

14 D. Q. Zhang, A. J. Duan, Z. Zhao and C. M. Xu, *J. Catal.*, 2010, **2**, 273–286.

15 Q. Tang, H. Xu, Y. Y. Zheng, J. F. Wang, H. S. Li and J. Zhang, *Appl. Catal., A*, 2012, **1**, 36–42.

16 H. S. Li, S. C. He, Q. Z. Jiao and K. N. Sun, *Appl. Catal., A*, 2013, **2**, 152–159.

17 R. Barakov, N. Shcherban and P. Yaremov, *J. Mater. Sci.*, 2016, **8**, 4002–4020.

18 Y. Fang and H. Hu, *J. Am. Chem. Soc.*, 2006, **33**, 10636–10637.

19 H. D. Wu, A. J. Duan, Z. Zhao, T. S. Li, P. Roel and X. F. Zhou, *J. Catal.*, 2014, **317**, 303–317.

20 G. Busca, *Chem. Rev.*, 2007, **107**, 5366–5410.

21 R. Weingarten, G. A. Tompsett, W. C. Conner and G. W. Huber, *J. Catal.*, 2011, **279**, 174–182.

22 J. Fan, C. Z. Yu, F. Gao, J. Lei, B. Z. Tian, L. M. Wang, Q. Luo, B. Tu, W. Z. Zhou and D. Y. Zhao, *Angew. Chem., Int. Ed.*, 2003, **27**, 3254–3258.

23 O. Ersen, J. Parmentier, L. A. Solovyov, M. Drillon and C. Pham-Huu, *J. Am. Chem. Soc.*, 2009, **49**, 16800–16806.

24 P. Du, P. Zheng, S. T. Song, M. H. Zhang and A. J. Duan, *RSC Adv.*, 2015, **2**, 1018–1026.

25 H. Li, F. Zhang, H. Yin, Y. Wan and Y. Lu, *Green Chem.*, 2007, **5**, 500–505.

26 C. A. Emeis, *ChemInform*, 1993, **38**, 347–354.

27 C. He, J. J. Li, P. Li, J. Cheng, Z. P. Hao and Z. P. Xu, *Appl. Catal., B*, 2010, **3–4**, 466–475.

28 J. L. Jiang, Y. Yang, C. Duan, Y. Xu, L. D. Feng, Xu. Gu and J. Chen, *Microporous Mesoporous Mater.*, 2012, **30**, 11–20.

29 G. Liu, F. X. Li, W. Wei, S. Liu and W. Jin, *Chem. Eng. J.*, 2011, **2**, 495–503.

30 Y. L. Su, J. Wang and H. Liu, *Langmuir*, 2002, **3**, 865–871.

31 Y. L. Su, X. F. Wei and H. Z. Liu, *J. Colloid Interface Sci.*, 2003, **2**, 526–531.

32 M. Almgren, P. Bahadur and M. Jansson, *J. Colloid Interface Sci.*, 1992, **1**, 157–165.

33 K. Michal, J. Mietek, K. A. Taewan and R. Ryoo, *Chem. Mater.*, 2003, **14**, 2815–2823.

34 J. C. P. Broekhoff and J. H. D. Boer, *J. Catal.*, 1968, **4**, 377–390.

35 J. Fan, C. Z. Yu and J. Lei, *J. Am. Chem. Soc.*, 2005, **31**, 10794–10795.

36 J. Tang, J. Liu, P. Wang, H. Zhong and Q. Yang, *Microporous Mesoporous Mater.*, 2010, **1**, 119–125.

37 F. Zaera, *ChemInform*, 2015, **3**, 7624–7663.

38 J. A. Z. Pieterse, S. Veefkind-Reyes, K. Seshan, L. Domokos and J. A. Lercher, *J. Catal.*, 1999, **2**, 518–520.

39 T. Kataoka and J. A. Dumesic, *ChemInform*, 1988, **42**, 66–79.

40 T. Klimova, L. Pena, L. Lizama, C. Salcedo and O. Y. Gutiérrez, *Ind. Eng. Chem. Res.*, 2008, **48**, 1126–1133.

41 G. Xiong, Z. Feng and J. Li, *J. Phys. Chem. B*, 2000, **104**, 3581–3588.

42 B. Riegel, I. Hartmann and W. Kiefer, *J. Non-Cryst. Solids*, 1997, **3**, 294–298.

43 Y. Borodko, J. W. Ager and G. E. Marti, *J. Phys. Chem. B*, 2005, **37**, 17386–17390.

44 S. Chytil, L. Haugland and E. A. Blekkan, *Microporous Mesoporous Mater.*, 2008, **1–3**, 134–142.

45 C. Hess, G. Tzolova-Müller and R. Herbert, *J. Phys. Chem. C*, 2007, **26**, 9471–9479.

46 E. Payen, J. Grimblot and S. Kasztelan, *ChemInform*, 1988, **14**, 6642–6648.

47 D. S. Kim, I. E. Wachs and K. Segawa, *J. Catal.*, 1994, **2**, 268–277.

48 M. A. Vuurman and I. E. Wachs, *J. Phys. Chem.*, 2002, **12**, 5008–5016.

49 T. E. Klimova, D. Valencia, J. A. Mendoza-Nieto and P. Hernández-Hipólito, *J. Catal.*, 2013, **11**, 29–46.

50 K. H. Choi, Y. Korai and I. Mochida, *Appl. Catal., A*, 2004, **2**, 229–236.

51 M. Adachi, C. Contescu and J. A. Schwarz, *J. Catal.*, 1996, **1**, 66–75.

52 X. L. Wang, H. Fang and Z. Zhao, *RSC Adv.*, 2015, **5**, 99706–99711.

53 W. K. Lai, W. J. Song and L. Q. Pang, *J. Catal.*, 2013, **13**, 80–91.

54 S. Jiang, Y. Zhou and S. Ding, *RSC Adv.*, 2016, **6**, 106680–106689.

55 B. Guichard, M. Roy-Auberger and E. Devers, *Catal. Today*, 2008, **1**, 97–108.

56 X. L. Wang, Z. Zhao and P. Zheng, *J. Catal.*, 2016, **344**, 680–691.